Geochemistry, Geophysics, Geosystems®

RESEARCH ARTICLE
10.1029/2023GC011390

High Sodium Solubility in Magnesiowüstite in Iron-Rich Deep Lower Mantle

Susannah M. Dorfman[1], Han Hsu[2], Farhang Nabiei[3,4], Marco Cantoni[5], James Badro[3,6], and Vitali B. Prakapenka[7]

[1]Department of Earth and Environmental Sciences, Michigan State University, East Lansing, MI, USA, [2]Department of Physics, National Central University, Taoyuan City, Taiwan, [3]Earth and Planetary Science Laboratory, Ecole polytechnique fédérale de Lausanne, Lausanne, Switzerland, [4]Now at Mediatek, Cambridge, UK, [5]Centre Interdisciplinaire de Microscopie Electronique, Ecole polytechnique fédérale de Lausanne, Lausanne, Switzerland, [6]Institut de Physique du Globe de Paris, Sorbonne Paris Cité, UMR CNRS, Paris, France, [7]Center for Advanced Radiation Sources, University of Chicago, Argonne, IL, USA

Abstract (Mg,Fe)O ferropericlase-magnesiowüstite has been proposed to host the majority of Earth's sodium, but the mechanism and capacity for incorporating the alkali cation remain unclear. In this work, experiments in the laser-heated diamond anvil cell and first-principles calculations determine the solubility of sodium and favorability of sodium incorporation in iron-rich magnesiowüstite relative to (Mg,Fe)SiO_3 bridgmanite. Reaction of Mg/(Mg + Fe) (Mg#) 55 and 28 olivine with NaCl at 33–128 GPa and 1600–3000 K produces iron-rich magnesiowüstite containing several percent sodium, while iron-rich bridgmanite contains little to no detectable sodium. In sodium-saturated magnesiowüstite, sodium number [Na/(Na + Mg + Fe)] is 2–5 atomic percent at pressures below 60 GPa and drastically increases to 10–20 atomic percent at deep lower mantle pressures. For these two compositions, there is no significant dependence of the results on Mg#. Our calculations not only show consistent results with experiments but further indicate that such an increase in solubility and partitioning of Na into magnesiowüstite is driven by the spin transition in iron. These results provide fundamental constraints on the crystal chemistry of sodium at lower-mantle conditions. If the sodium capacity of (Mg,Fe)O is not strongly dependent on Mg#, (Mg,Fe)O in the lower mantle may have the capacity to store the entire sodium budget of the Earth.

Plain Language Summary Sodium is among the most abundant elements on the Earth, but where it can be stored in the Earth's largest layer, the lower mantle, has not been understood. Whether sodium dissolves into the most common minerals in the mantle affects the interpretation of the Earth's composition and structure. This study uses experiments and computer simulations of reactions of sodium with the two most common minerals in the lower mantle to determine how much sodium can be dissolved in the mantle. Both methods show that enough sodium can dissolve into magnesium-iron oxide, called ferropericlase or magnesiowüstite, to store all of the Earth's sodium budget. The amount of sodium that dissolves into this mineral increases with depth in the Earth because of a change in the arrangement of electrons around iron, which takes part in the chemical reaction with sodium.

Key Points:

- Experiments show that sodium strongly partitions to (Mg,Fe)O magnesiowüstite and is not incorporated in bridgmanite
- Sodium is soluble in iron-rich (Mg,Fe)O in the deep lower mantle at multiple percent level
- First-principle calculations show that spin transition in (Mg,Fe)O drives a pressure-driven increase in sodium solubility

Supporting Information:

Supporting Information may be found in the online version of this article.

Correspondence to:

S. M. Dorfman and H. Hsu,
dorfman3@msu.edu;
hanhsu@ncu.edu.tw

Citation:

Dorfman, S. M., Hsu, H., Nabiei, F., Cantoni, M., Badro, J., & Prakapenka, V. (2024). High sodium solubility in magnesiowüstite in iron-rich deep lower mantle. *Geochemistry, Geophysics, Geosystems*, *25*, e2023GC011390. https://doi.org/10.1029/2023GC011390

Received 8 DEC 2023
Accepted 16 MAY 2024

Author Contributions:

Conceptualization: Susannah M. Dorfman, Han Hsu
Formal analysis: Susannah M. Dorfman, Han Hsu
Investigation: Susannah M. Dorfman, Han Hsu, Farhang Nabiei
Methodology: Susannah M. Dorfman, Han Hsu, Farhang Nabiei, Marco Cantoni, Vitali B. Prakapenka
Resources: Marco Cantoni, James Badro, Vitali B. Prakapenka

1. Introduction

Mantle composition and its variation with region and depth is critical for interpreting seismic wave speeds and resolving questions of planet-scale volatile cycles, mantle dynamics and mixing. Heterogeneous distribution of alkali cations in the mantle is related to the subduction and mixing of sediment and basalt, and because these cations are mobile in mantle fluids they may follow volatile cycles through the deep Earth (Manning, 2004). Alkali cations affect the stability, melting behavior, and release of volatiles that fuel arc volcanism and travel through the mantle within carbonates and brines. Diamond inclusions indicate that brines likely have a subducted source and flow through other mantle lithologies (Weiss et al., 2022). Na-Ca carbonates host oxidized carbon in Earth's transition zone (Rashchenko et al., 2020), and because they reduce the solidus of carbonate-rich rocks they control the depth of carbon cycling in the mantle (Rohrbach & Schmidt, 2011). Melting of these alkali carbonates during hot subduction may also produce NaCl and KCl crystallizing from fluids, resulting in delivery of solid alkali chlorides to the lower mantle (Chen et al., 2023). The presence of dissolved alkali cations and chloride in brine has a significant impact on electrical conductivity of mantle fluids (Pommier, 2014). Although the ~0.26

Visualization: Susannah M. Dorfman, Han Hsu
Writing – original draft: Susannah M. Dorfman, Han Hsu
Writing – review & editing: James Badro

weight percent sodium in average mantle (McDonough & Sun, 1995) may not be detectable using seismic methods, mid-ocean-ridge basalt contains 2.71–2.83 wt% Na_2O (Gale et al., 2013). Oceanic crust subducted into the mantle may form piles at the base of the transition zone (e.g., Bissig et al., 2022; Feng et al., 2021; Tauzin et al., 2022) and lowermost mantle (Brandenburg & van Keken, 2007; Christensen & Hofmann, 1994; Jones et al., 2020; Mulyukova et al., 2015; Nakagawa et al., 2010; Tackley, 2011). Recycled basalt is estimated to comprise ∼2%–20% of the deep mantle (Sobolev et al., 2007). Although the inefficiency of solid-state mixing through mantle convection suggests grain-scale equilibrium between basalt and harzburgite is not reached throughout most of the mantle (Ballmer et al., 2015; Xu et al., 2008), intermediate lithologies may equilibrate at subduction conditions where there is partial melt or fluid (Hofmann & Hart, 1978). Partial melting may be common near the core-mantle boundary for a wide range of compositions including subducted basalt, pyrolite, chondrite, and iron-rich lithologies (Andrault et al., 2011, 2014; Caracas et al., 2019; Kim et al., 2020; Pradhan et al., 2015; Tateno et al., 2014; Williams & Garnero, 1996). Tracking sodium storage and cycling through the mantle thus allows insights into fate of basaltic crust, mantle metasomatism, the heterogeneous core-mantle boundary region, and deep-sourced volcanism.

Recent work aims to improve thermodynamic modeling of the chemical behavior of alkali cations to successfully model abundance and composition of mantle phases for arbitrary mantle-relevant lithologies (Stixrude & Lithgow-Bertelloni, 2022). These models rely on experimental data on phase equilibria and element partitioning. Experimental measurements of sodium concentrations in minerals in mantle-relevant chondritic, pyrolitic or harzburgitic compositions have been limited to modest lower mantle pressures up to ∼47.4 GPa and have not systematically examined the crystal chemistry of sodium incorporation (Brey et al., 2004; Gasparik, 2000; Hirose, 2002; Irifune, 1994; Irifune et al., 2010; Kubo et al., 2008; Wood, 2000). Experiments on basaltic compositions show that separate Na,Al-rich phases can store ∼5–13 wt% Na_2O (Hirose et al., 2005; Kesson et al., 1994; Litasov & Ohtani, 2005; Ono et al., 2001; Ricolleau et al., 2010). Depending on concentrations of potassium and sodium and pressure/temperature conditions, the aluminous phase may be garnet, hexagonal "new aluminous phase," or orthorhombic calcium-ferrite-type phase (Kato et al., 2013; Miyajima et al., 2001; Rogmann et al., 2024). These Na,Al-rich phases are not present in harzburgite or pyrolite compositions in the lower mantle (Irifune, 1994; Ishii et al., 2019). The stability of Na,Al-rich phases in compositions between pyrolite and basalt and solubility limit for Na in major mantle phases is not well-constrained. Introducing the sodium ion into crystal structures of major mantle minerals (Mg,Fe) $(Al,Si)O_3$ bridgmanite, (Mg,Fe)O ferropericlase, and $CaSiO_3$ davemaoite requires balancing charge differences by adding defects or pairing substitution with trivalent cations such as ferric iron (Fe^{3+}). These chemical reactions may depend on compositional variables including oxygen fugacity and concentration of iron and aluminum as well as mantle pressure/temperature conditions due to the effects of vacancies and pressure-induced electronic changes in iron on mineral density and enthalpy (Badro, 2014; H. Fei et al., 2021).

In this study, we combine spectroscopic and computational approaches to examine Na-incorporation in an iron-rich olivine stoichiometry assemblage of (Fe,Mg)O magnesiowüstite and $(Mg,Fe)SiO_3$ bridgmanite crystallized at conditions reaching lowermost mantle pressures and temperatures. This composition allows us to test the effects of iron concentration and pressure on crystal chemistry of the major mantle phases in dense heterogeneities near Earth's core-mantle boundary. An Al-free system is ideal to examine the effects of the electronic configuration of iron on the crystal chemistry of mantle phases. The results provide in-depth information to update models of the stability and thermodynamic properties of mantle phase assemblages.

2. Materials and Methods

The preparation and analysis of experiments on (Fe,Mg)O magnesiowüstite in contact with NaCl in the laser-heated diamond anvil cell was described in Dorfman et al. (2021). Starting materials are synthetic Mg/(Mg + Fe) or Mg# 55 and 28 (Fe# 45 and 72) olivine within a NaCl pressure-transmitting and insulating medium. Starting materials were reacted by laser heating for 10–60 min at 33–122 GPa and 1980–3000 K at the GeoSoilEnviroCARS sector of the Advanced Photon Source (APS), Argonne National Laboratory (Prakapenka et al., 2008), and the Ecole Polytechnique Federale de Lausanne (EPFL) (Dorfman et al., 2021) (Table 1). Pressures were determined at ambient temperature before heating by Raman spectroscopy of the diamond anvil (Akahama & Kawamura, 2006) or the equation of state of the NaCl medium (Dorfman et al., 2012). Before and after heating, up to ∼2 GPa difference in pressure is observed due to change in crystal structure and non-hydrostatic stress in the sample and NaCl medium. Pressure at ambient temperature is systematically lower than

Table 1
Summary of Experimental Run Conditions and Observations

Sample Mg#	Pressure (GPa)	Temperature (K)	Heating time (min)	Typical grain size (nm)	XRD?	Observed phases
55	40	2000	10	100–300	Yes	Mws, Bdg, SiO_2
55	62	2000	15	50–100	Yes	Mws, Bdg, Cl
55	71	2440	20	50–100	Yes	Mws, Bdg
55	89	2600	15	60–100	Yes	Mws, Bdg, Cl
28	33	1980	15	30–100	Yes	Mws, Bdg, SiO_2, Cl
28	39	2000	30	50–500	No	Mws, Bdg, SiO_2
28	48	1900	15	50–100	Yes	Mws, Bdg, Cl
28	52	2000	30	10–400	No	Mws, Bdg, Fe, Cl
28	82	2000	20	50–100	No	Mws, Bdg, Fe, Cl
28	89	2200	35	40–100	Yes	Mws, Bdg, pPv, Cl
28	97	3000	60	100+	No	Mws, Bdg/pPv?, Cl
28	122	2500	30	30–100	No	Mws, Bdg + pPv?, SiO_2, Cl

Note. Experiments for which X-ray diffraction (XRD) data were obtained were carried out at beamline 13-ID-D of the GSECARS sector of the APS, while other experiments carried out at EPFL were observed ex situ only. For observed phases, Bdg = bridgmanite, pPv = post-perovskite, Mws = magnesiowüstite, SiO_2 = stishovite or other silica polymorph, Fe = metallic iron, and Cl = iron or magnesium chloride at grain boundaries. "Bdg + pPv" observations for samples synthesized above 89 GPa are marked with "?" due to lack of in situ structural information.

pressure during laser heating by ∼7–10 GPa for these materials due to thermal pressure (Dorogokupets & Dewaele, 2007). These sources of uncertainty are larger than reported ∼1% uncertainty of the pressure scales. After heating, synchrotron X-ray diffraction carried out at beamline 13-ID-D of the APS indicates that all experiments produced magnesiowüstite in the cubic B1 structure. Depending on conditions, X-ray diffraction shows that (Mg,Fe)O also coexists with (Mg,Fe)SiO_3 bridgmanite, SiO_2, and/or (Mg,Fe)SiO_3 post-perovskite (Table 1).

Distributions of elements in recovered samples were determined by energy-dispersive X-ray (EDX) spectroscopic mapping in a FEI Technai Osiris analytical transmission electron microscope (ATEM) after liftout using a Zeiss NVision dual focused Ga^+ ion beam and scanning electron microscope, both at the Interdisciplinary Center for Electron Microscopy, EPFL (Figure 1). NaCl was removed from the silicate sample by dissolution by a drop or two of deionized water, and may remain enriched on the sample surface. Each area of interest was coated with a carbon layer before Ga^+ milling at 30 kV and 1.5–27 nA. After transfer to a Cu TEM grid, sections were thinned at 30 kV and 300 pA to 100–200 nm for electron transparency, then cleaned and polished at 5 kV and 80 pA with the Ga^+ beam oriented at a 5° angle to the surface. Imaging and EDX were carried out with electron beam voltage 200 kV. EDX spectra were recorded at 10,000–50,000 counts/s with pixel dwell time 50 µs for ∼10 min total for each map. EDX analysis in the ATEM allowed the identification of ∼10-nm-scale grains of metallic iron and an additional Cl-bearing phase (Table 1). Compositions for individual grains were obtained using ESPRIT Quantax software (Bruker) by summing spectra obtained within ∼100-nm-diameter selected areas. Grains were selected for composition analysis near the center of heated spots to minimize the effects of temperature gradients during laser heating on chemistry.

To model Na partitioning between Fe-rich wüstite and bridgmanite at lower-mantle pressures, we performed first-principles calculations based on density functional theory (DFT) using the Quantum ESPRESSO codes (Giannozzi et al., 2009, 2017). Structures of all relevant mineral phases are fully optimized at various pressures, and the calculation results are fitted to the third-order Birch–Murnaghan equation of state (Birch, 1978). In our calculations, GBRV ultrasoft pseudopotentials (Garrity et al., 2014) are adopted. To account for the on-site Coulomb interactions of Fe 3*d* electrons, we use the local density approximation + Hubbard *U* (LDA + *U*) method, with $U = 4$ eV for Fe in all spin/oxidation states and all lattice sites. Further details for our calculations, including the cut-off energy (60 Ry) and the **k**-point mesh ($6 \times 6 \times 4$ for 20-atom $NaFe_3Si_4O_{12}$ and $Fe_4Si_4O_{12}$, $10 \times 10 \times 10$ for 4-atom Fe_2O_2 and $FeNaO_2$, see also Section 4), can be found in the example input/output files described in the Open Research section.

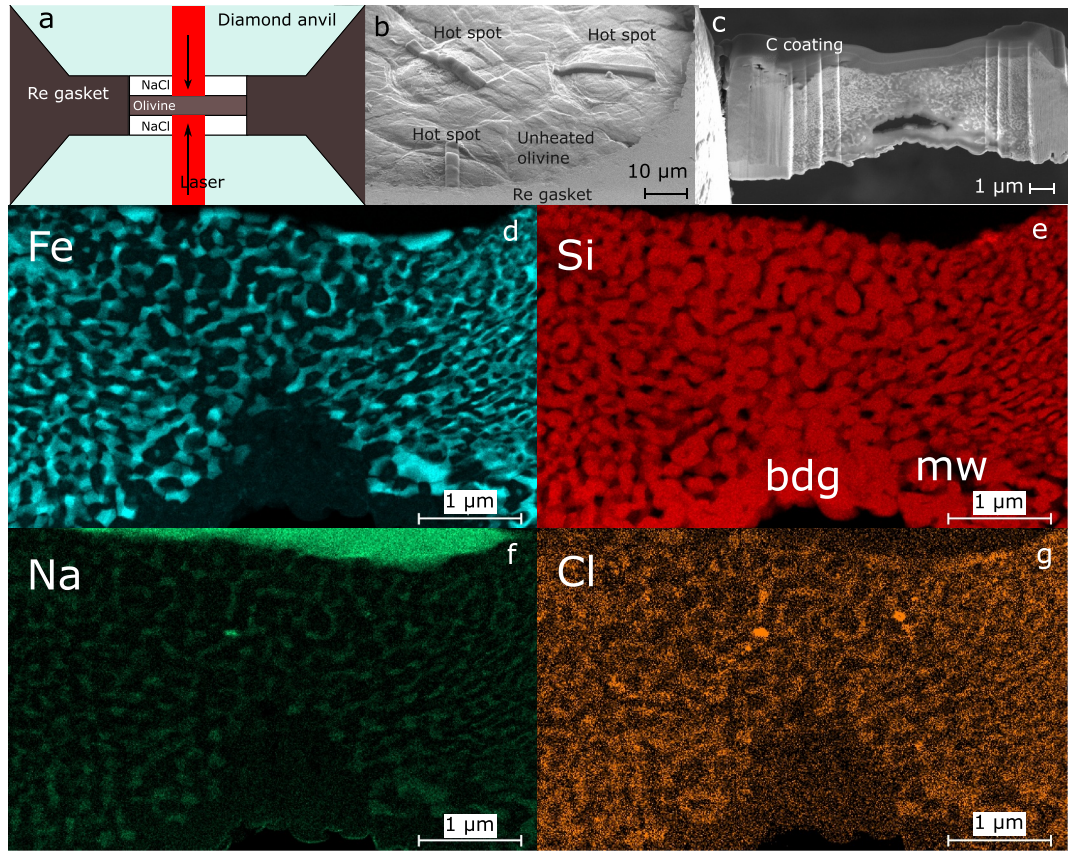

Figure 1. (a) Schematic cartoon for laser-heating of layered NaCl-olivine-NaCl sample in the diamond anvil cell. (b) After recovery to 1 bar and removal of NaCl with deionized water, surface topography of the olivine observed by secondary electron imaging indicates heated spots, which are coated with a layer of protective carbon. (c) Cross section of Fa45 (Mg#55) sample recovered from 40 GPa to 2000 K cut and lifted out by focused Ga^+ ion beam. Void may represent decompression or fluid pocket due to hygroscopic NaCl medium. Bridgmanite enrichment near the void and elongated texture at edges of the heated spot may be due to axial and radial temperature gradients during laser heating. (d–g) Energy-dispersive X-ray spectroscopy maps for this sample for Fe (cyan), Si (red), Na (green), and Cl (orange).

3. Experimental Observations of Na-Saturated Olivine Composition in the Lower Mantle

EDX spectra obtained from regions within (Fe,Mg)O grains consistently exhibit a Na peak, while spectra from $(Mg,Fe)SiO_3$ have a weaker or insignificant Na peak (Figure 2). In element maps (Figures 1 and 3), (Fe,Mg)O grains appear enriched in iron and lack silicon (which makes magnesium also appear relatively enriched), whereas $(Mg,Fe)SiO_3$ always contains silicon and relatively less iron. Sodium enrichment is correlated with (Fe,Mg)O. These observations demonstrate that sodium partitions strongly into (Fe,Mg)O and is not incorporated into $(Mg,Fe)SiO_3$.

Although the insulating medium in these experiments is a source of both Na and Cl, we observe a clear contrast in the incorporation of Na in (Fe,Mg)O relative to Cl. While elemental maps for Na and Cl both show enrichment in (Fe,Mg)O regions relative to silicate regions (Figures 1f and 1g), the Cl concentration is much lower than the Na concentration. No significant Cl peak is observed in either the oxide or the silicate in Figure 2. The calculated Cl concentration in (Fe,Mg)O grains is an order of magnitude smaller than the concentration of Na, 0.2 atomic percent on average (see Data Set S1). At higher zoom, element maps show that while Na is dissolved throughout (Fe,Mg)O grains, Cl is concentrated at grain boundaries between (Fe,Mg)O and $(Mg,Fe)SiO_3$ (Figure 3). Grain boundary chloride film is observed in almost every recovered sample (Table 1). Mg appears depleted at these grain boundaries, while no clear contrast in Fe or Si can be identified. Due to the small grain size, the composition of this Cl-rich film cannot be quantified, and no additional chloride phases were identified in diffraction data. The

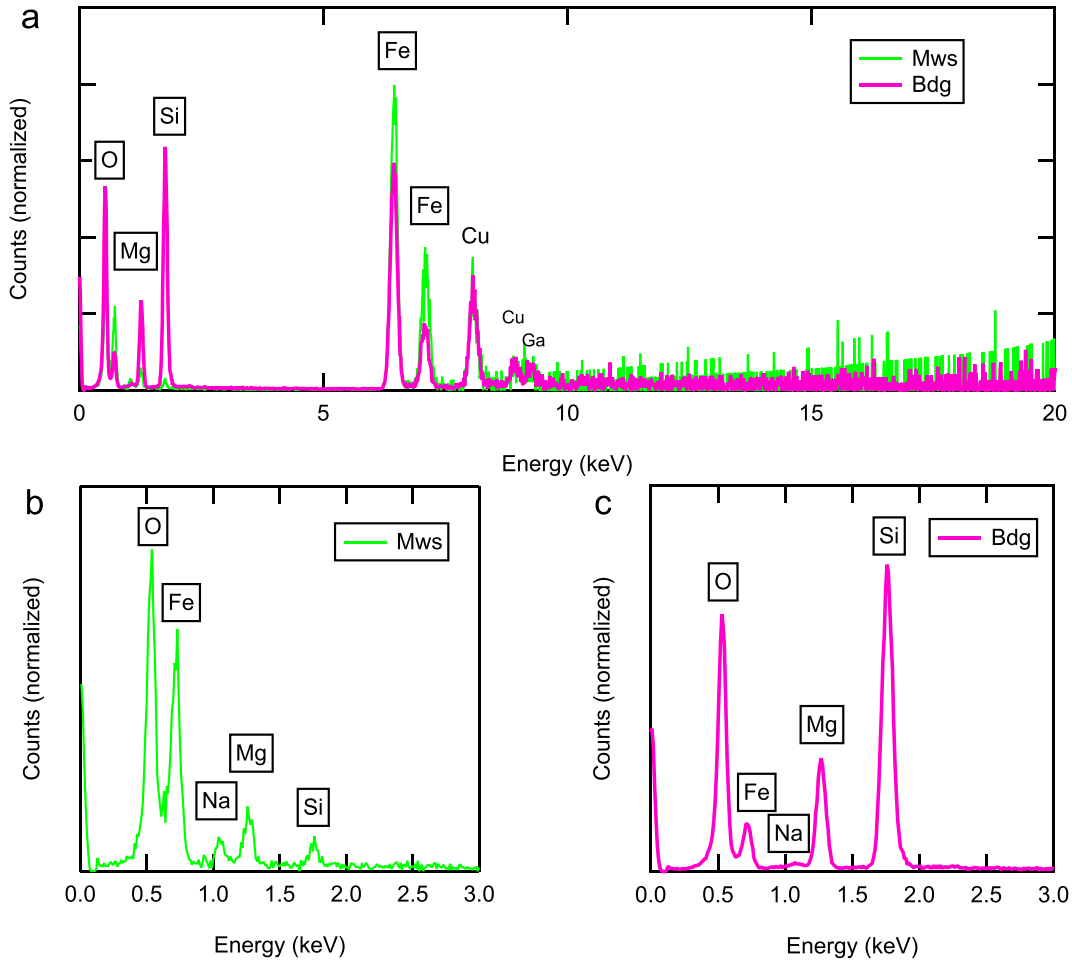

Figure 2. Example energy-dispersive X-ray spectra obtained from grains of magnesiowüstite (a, b) and bridgmanite (a, c) formed in Fa72 (Mg#28) composition at 52 GPa and 2000 K. If present, Cl would be observed at 2.621 keV.

formation of the accessory Cl-rich phase allows the oxide and silicate to be saturated in Na without incorporating Cl. The absence of Cl in (Fe,Mg)O also demonstrates that Cl does not provide charge balance for substitution of Na into the structure. Occasionally, a grain of NaCl can also be identified within the silicate sample, such as the bright co-located Na and Cl spots near the sample center in Figures 1f and 1g.

Because grain sizes for recovered DAC samples can be smaller than the 100-nm thickness of the lamellae, it is important to consider whether we have sufficient spatial resolution to separate the compositions of (Fe,Mg)O, (Mg,Fe)SiO_3, and possible films at grain boundaries, and quantify Na-incorporation in these phases. (Fe,Mg)O EDX spectra also typically exhibit a weak Si peak (Figure 2a) indicating that signal from the silicate bridgmanite is contributing to the observed spectrum. The measured concentration of Na decreases with increasing Si (Figure 4a), consistent with mixing between overlapping Na-enriched (Fe,Mg)O and Na-free (Mg,Fe)SiO_3. The concentration of Na in (Fe,Mg)O can thus be obtained from the *y*-intercept of a line fit to this mixing trend for Na versus Si measured in magnesiowüstite grains. For (Mg,Fe)SiO_3 grains, Na concentration is too low (Figure 4b) to reliably separate from contamination from neighboring grains, so we consider Na concentration in bridgmanite and post-perovskite below significance.

The three samples recovered from 33, 82, and 122 GPa included in Figure 4 also illustrate a broader trend of increasing Na-concentration in grains recovered from higher pressure and higher temperature experiments (Figure 5). All samples compressed to maximum pressures less than 80 GPa contain ~2%-5% Na/(Ng + Mg + Fe) in (Fe,Mg)O. From 80 to 120 GPa, Na/(Ng + Mg + Fe) in (Fe,Mg)O increases dramatically to 6%–10% and as high as 20 ± 1.0%. The three highest concentrations of sodium are also observed in the samples heated to the

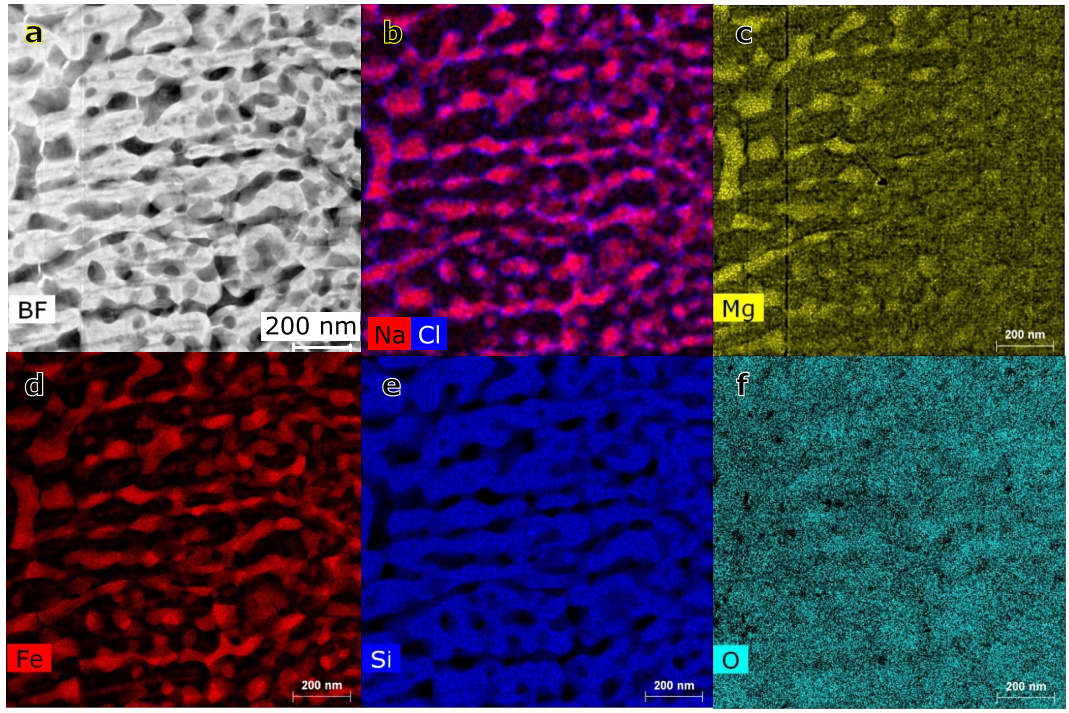

Figure 3. (a) Bright field STEM image of Fa45 (Mg#55) after recovery from 62 GPa, 2000 K. (b) Overlaid element maps of Na (red) and Cl (blue) indicate that Na is incorporated within (Fe,Mg)O grains, while Cl is concentrated at grain boundaries. (c) Mg (yellow), (d) Fe (red), (e) Si (blue) and (f) O (cyan) maps highlight (Fe,Mg)O and (Mg,Fe)SiO_3 grains.

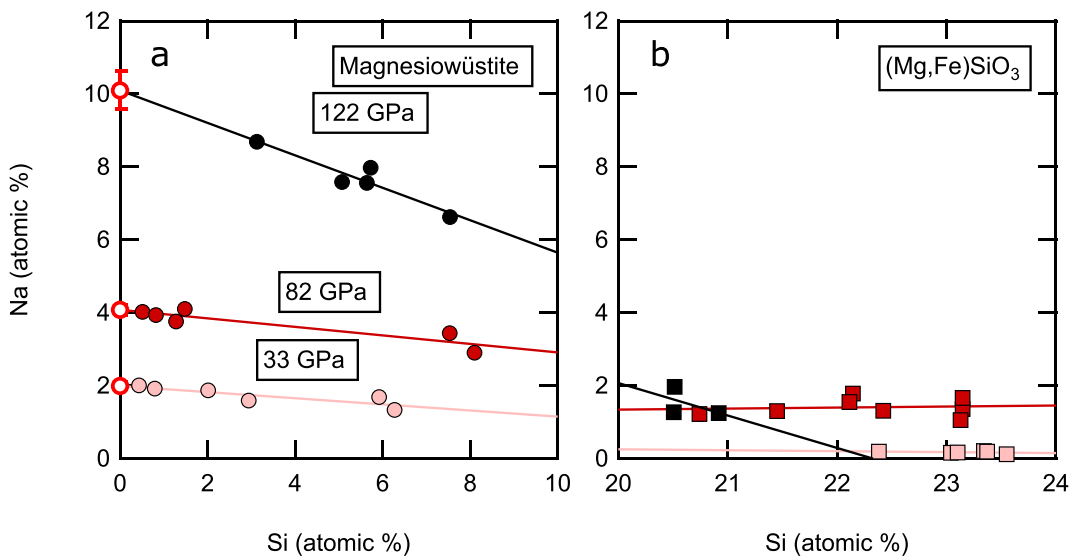

Figure 4. In recovered samples from selected experiments on the Fa72 (Mg#28) composition, (a) sodium concentration in (Fe,Mg)O grains obtained from EDX spectroscopy in STEM plotted relative to silicon concentration, which indicates overlap with (Mg,Fe)SiO_3 grains due to small grain sizes, and (b) analogous observations for sodium concentration in (Mg,Fe)SiO_3 grains. Lines are least-squares fits. Open circles with 1-σ error bars indicate y-intercepts of line fits with uncertainty and represent the estimated concentration of sodium in (Fe,Mg)O. For 33 and 82 GPa samples, uncertainty in the y-intercept is smaller than the symbol size. For (Mg,Fe)SiO_3, observed sodium concentration represents an upper bound due to potential overlap with (Fe,Mg)O grains.

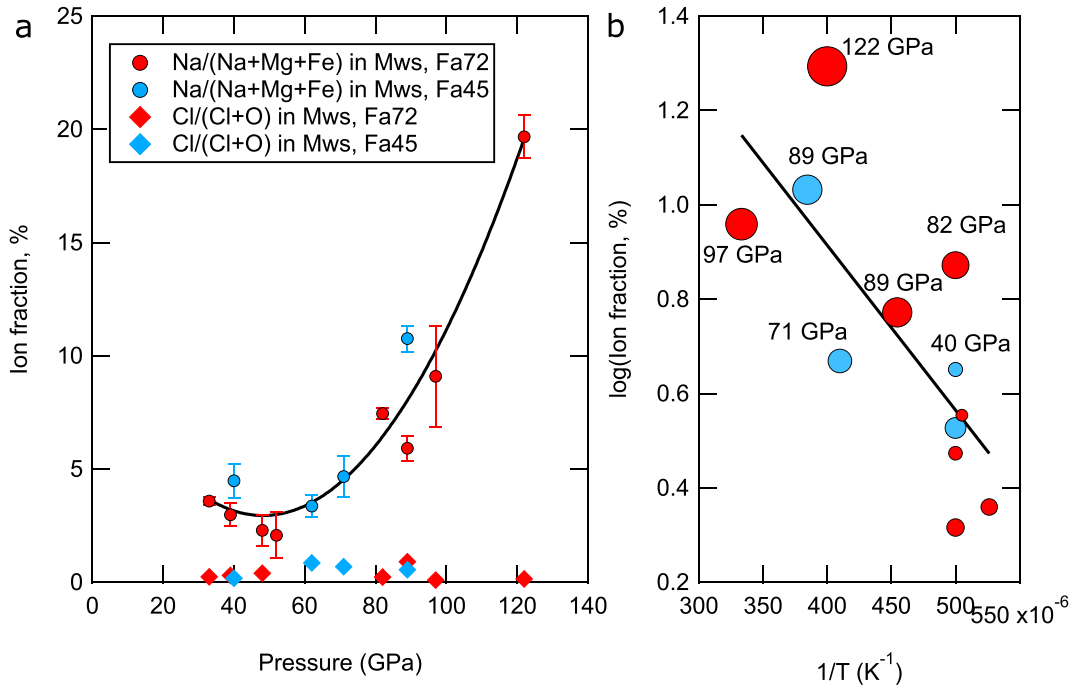

Figure 5. (a) Sodium concentration normalized to total cations, Na/(Na + Mg + Fe) in (Fe,Mg)O (circles) in Fa45 (Mg#55) and Fa72 (Mg#28) compositions, with polynomial least-squares fit (black line); Cl concentration normalized to total anions, Cl/(Cl + O) (diamonds). (b) Logarithm of Na/(Na + Mg + Fe) concentration in (Fe,Mg)O as a function of inverse temperature, with least-squares linear fit (black line). Symbol size in this figure is proportional to pressure from 33 to 122 GPa.

highest temperatures, 2500–3000 K (Table 1, Figure 5b). Relatively higher temperatures were applied to higher pressure experiments representing deep mantle conditions to approximate a geotherm. The logarithm of observed sodium concentration is correlated with 1/T, consistent with high temperature promoting entropic mixing of Na into the (Fe,Mg)O structure. However, defect concentration is not fully explained by temperature alone, as illustrated by the wide range of Na concentration observed at different pressures but similar temperatures ~2000 and ~2500 K. Differences in Mg# do not have a significant effect on incorporation of Na. In Figure 5, we fit effects of temperature and pressure on Na/(Na + Mg + Fe) to single trends for both Fa45 (Mg#55) and Fa72 (Mg#28) samples. Due to partitioning of Fe between the two major phases, in Fa45 (Mg#55) samples Mg# in magnesiowüstite ranges from 20 to 35, while in Fa72 (Mg#28), Mg# in magnesiowüstite is 13 or less (Dorfman et al., 2021). Any effect of variable Mg# in this Fe-rich system on Na-incorporation in (Fe,Mg)O is small relative to the increase in solubility of Na due to pressure above 80 GPa and temperature above 2000 K.

4. First-Principles Modeling of Na Partitioning at Lower-Mantle Pressure

To elucidate the partitioning of Na into wüstite relative to Fe-rich bridgmanite and increase in Na solubility in wüstite with pressure indicated by experiments, we performed first-principles static LDA + U calculations to compute the formation enthalpy (ΔH^f) of the following model reaction, which describes Na substitution and partitioning between FeO and $FeSiO_3$ bridgmanite: $2Fe^{2+}O + (NaFe^{3+}Fe^{2+}_2)Si_4O_{12} \rightleftharpoons (NaFe^{3+})O_2 + 4Fe^{2+}SiO_3$. By definition, formation enthalpy is the relative enthalpy between the products and the reactants, that is, $\Delta H^f \equiv [H(NaFeO_2) + H(4*FeSiO_3)] - [H(2*FeO) + H(NaFe_3Si_4O_{12})]$; it can thus be re-written as the difference between the defect formation enthalpies of FeO and $FeSiO_3$: $\Delta H^f = [H(NaFeO_2) - H(2*FeO)] - [H(NaFe_3Si_4O_{12}) - H(4*FeSiO_3)]$. By assuming ideal mixing, as outlined in Hernández et al. (2013) and Townsend et al. (2016), partition coefficient of Na between these two phases $D_{Na}^{wu/bdg} \equiv [Na]_{wu}/[Na]_{bdg} \approx \exp(-\Delta G^f/k_BT)$, where ΔG^f is free energy of formation, in which lattice vibrational free energy is included. Without the inclusion of lattice vibration, ΔG^f reduces to ΔH^f, and partition coefficient can be estimated via formation enthalpy

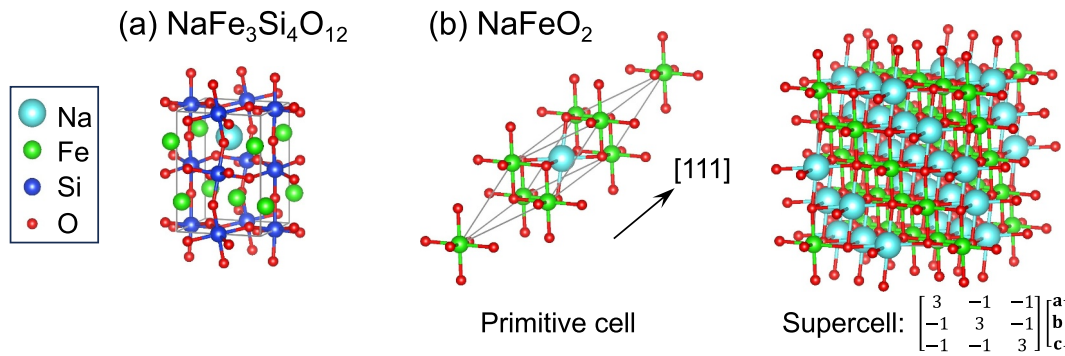

Figure 6. Atomic structure of (a) 20-atom $NaFe_3Si_4O_{12}$ and (b) 4-atom $NaFeO_2$. In panel (b), a supercell of $NaFeO_2$ is also plotted to better showcase the resemblance of this structure to rB1 FeO.

(Hernández et al., 2013): $D_{Na}^{wu/bdg} \approx \exp(-\Delta H^f/k_BT)$. Clearly, when $\Delta H^f < 0$, the partition coefficient would be large, and Na partitioning would favor FeO rather than $FeSiO_3$.

In our calculation, Na-bearing $FeSiO_3$ bridgmanite is modeled by 20-atom $NaFe_3Si_4O_{12}$ cells (Figure 6a). For FeO, both the cubic B1 (rock-salt) and rhombohedrally distorted B1 (rB1) structures are considered, as rB1 is the stable structure of FeO at room temperature up to ∼100 GPa (Fischer et al., 2011; Ozawa et al., 2010), and substitution of Mg stabilizes the cubic B1 structure: X-ray diffraction indicates that experiments discussed in this study produced cubic B1 (Dorfman et al., 2021). The structure of Na-bearing FeO is obtained by substituting one of the Fe atoms in (r)B1 antiferromagnetic (AFM) FeO (4-atom cell). The resultant structure, shown in Figure 6b, is known as α-$NaFeO_2$, with alternating Fe and Na layers parallel to the (111) plane. Since (Mg,Fe)O magnesiowüstite undergoes a spin transition at lower-mantle conditions (Badro, 2014; Lin et al., 2013), both high-spin (HS) and low-spin (LS) states of FeO and $NaFeO_2$ are considered here. In contrast, Fe^{2+}/Fe^{3+} in the dodecahedral site of bridgmanite remains HS throughout the lower-mantle pressure (Hsu et al., 2011; Hsu, Umemoto, Blaha, & Wentzcovitch, 2010; Hsu, Umemoto, Wu, & Wentzcovitch, 2010; Hsu & Wentzcovitch, 2014; Hsu & Yu, 2012). In the present calculation, we also find that the enthalpy of LS $NaFe_3Si_4O_{12}$ is higher than the HS state by several eV/cell. Therefore, we focus our discussion on HS $FeSiO_3$ and $NaFe_3Si_4O_{12}$. For pure FeO, AFM ordering is adopted; for other phases, ferromagnetic (FM) ordering is adopted.

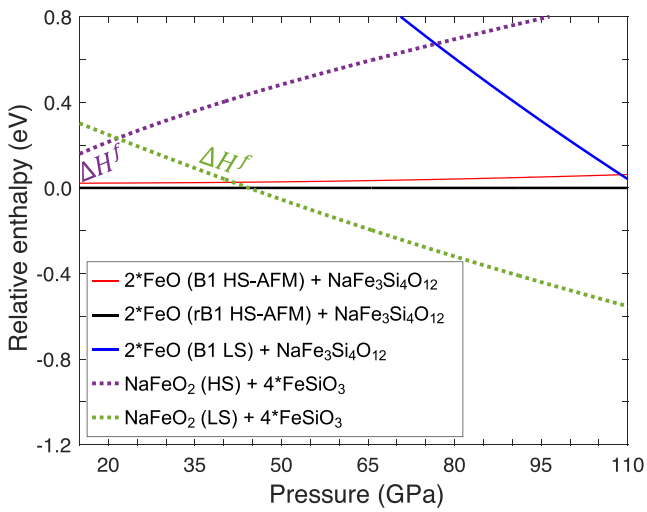

Figure 7. Relative enthalpies of (2*FeO + $NaFe_3Si_4O_{12}$) and ($NaFeO_2$ + 4*$FeSiO_3$) in various possible spin and structural states. An enthalpy crossing of ($NaFeO_2$ + 4$FeSiO_3$) caused by the spin transition of Fe^{3+} in $NaFeO_2$ occurs at 21.6 GPa. For $P > 21.6$ GPa, the formation enthalpy ΔH^f decreases with pressure and becomes negative at 44.4 GPa, indicating Na partitioning favors FeO for $P > 44.4$ GPa.

In Figure 7, relative enthalpies of the reactants (2*FeO + $NaFe_3Si_4O_{12}$, solid lines) and products ($NaFeO_2$ + 4*$FeSiO_3$, dotted lines) are plotted. Enthalpy of 2*FeO (rB1 HS-AFM) + $NaFe_3Si_4O_{12}$ (indicated as the black solid line) is used as the reference, for this combination is the most energetically favorable at pressure $P < 44.4$ GPa. Cubic B1 HS-AFM FeO is slightly less favorable, evident from the slightly higher enthalpy of 2*FeO (B1 HS-AFM) + $NaFe_3Si_4O_{12}$ (red thin solid line). B1 LS FeO is highly unfavorable (see blue solid line) and is thus of no concern. Our results for rB1/B1 FeO are consistent with the LDA + U calculation by Sun et al. (2020), which adopted a different set of U parameters. At $P < 44.4$ GPa, relative enthalpies of the products ($NaFeO_2$ + 4*$FeSiO_3$, dotted lines) are positive, regardless of the spin state of $NaFeO_2$. Remarkably, while the enthalpy of $NaFeO_2$ (HS) + 4*$FeSiO_3$ (purple dotted line) increases with pressure, a crossing with $NaFeO_2$ (LS) + 4*$FeSiO_3$ (green dotted line) occurs at 21.6 GPa, indicating iron spin transition in $NaFeO_2$, from HS Fe^{3+} ($S = 5/2$) to LS Fe^{3+} ($S = 1/2$). This predicted spin-transition pressure, likely being underestimated due to the choice of the $U = 4$ eV (Hsu, 2017; Hsu & Huang, 2016), is comparable to conditions of electronic spin transitions observed in experiments on iron-rich lower mantle phases (Dorfman et al., 2015; Y. Fei et al., 2007; Mao et al., 2015; Speziale et al., 2007). After the HS–LS transition, relative enthalpy of $NaFeO_2$ (LS) + 4*$FeSiO_3$, namely, the formation enthalpy ΔH^f, decreases with pressure and becomes negative at 44.4 GPa, indicating Na

partitions into FeO more than $FeSiO_3$ for $P > 44.4$ GPa. Upon further compression, ΔH^f further decreases, indicating $[Na]_{wu}/[Na]_{bdg}$ further increases. These calculation results show great agreement with our experiments: starting ~60 GPa, Na concentration in Fe-rich wüstite increases with pressure, while that in bridgmanite remains insignificant.

5. Discussion

Although this study examines iron-enriched compositions, our experimental observations and computational evidence that sodium is concentrated in (Fe,Mg)O relative to $(Mg,Fe)SiO_3$ are qualitatively similar to observations in previous studies of lower mantle phases in ultramafic lithologies (Brey et al., 2004; Gasparik, 2000; Hirose, 2002; Irifune, 1994; Irifune et al., 2010; Kubo et al., 2008; Wood, 2000). Ferropericlase synthesized in chondritic, pyrolitic or harzburgitic compositions at 19–47.4 GPa contains ~1 wt% Na_2O, consistent with nearly all available Na partitioning strongly into the oxide (Gasparik, 2000; Hirose, 2002; Irifune, 1994; Irifune et al., 2010; Wood, 2000). Results for sodium partitioning between phases in experiments carried out at higher pressures have been inconclusive because compositional analysis for individual phases typically suffers from small grain sizes (Tateno et al., 2014) and analytical uncertainty (Kubo et al., 2008). In contrast to this study and most previous experiments, a Na-saturated, Fe,Al-free composition at shallow lower mantle pressures and temperatures transformed to Na-free periclase in contact with bridgmanite containing as much as 0.67 wt% Na_2O and anhydrous sodium phase X ($Na_2Mg_2Si_2O_7$) (Matrosova et al., 2020). The difference between these experimental observations may be explained by differences in bulk composition and the mechanism of sodium incorporation in the oxide.

In general, incorporation of sodium in the (Fe,Mg)O or $(Mg,Fe)SiO_3$ structures requires compensating the charge difference between monovalent sodium and divalent iron and magnesium by either replacing oxygen with a lower charge chloride ion or vacancy, or pairing the substitution of sodium with hydroxyl or incorporation of a trivalent ion such as ferric iron or aluminum. Our computational work focuses on the paired substitution of sodium with ferric iron. In experiments, the absence of Fe^{3+} from the starting material, absence of Cl in the oxide, and formation of a separate chloride phase at grain boundaries (Figure 3) require reactions that separate the Na ion and oxidize iron. Experimental observations can be explained by the following reactions:

$$2NaCl + \left(Fe^{2+},Mg\right)O \leftrightarrow Na_2O + \left(Mg,Fe^{2+}\right)Cl_2 \quad (1)$$

$$Na_2O + \left(Fe^{2+},Mg\right)O \leftrightarrow Na_x\left(Fe^{2+},Mg\right)_{1-x}O_{1-x/2} \quad (2)$$

$$Na_2O + 3FeO \leftrightarrow 2NaFe^{3+}O_2 + Fe \quad (3)$$

Although X-ray diffraction and STEM analysis were unable to isolate the composition and structure of chloride films, substitution of Na for Mg and Fe is likely to produce $MgCl_2$ and/or $FeCl_2$, as shown in Reaction 1. This exchange reaction produces Na_2O which may then enter the oxide by a oxygen vacancy mechanism as Reaction 2.

ATEM is unable to provide measurements of oxygen concentration with sufficient accuracy to directly test for the presence of oxygen vacancies in experiments presented here. However, the complexity of the dependence of observed sodium defect concentration in the oxide on pressure and temperature (Figure 5) likely indicates that different substitution mechanisms operate under different mantle pressure/temperature conditions. Oxygen vacancies are unlikely to be the dominant mechanism supporting sodium incorporation in (Fe,Mg)O at higher pressures. In ferropericlase, oxygen vacancies paired with trivalent iron as $MgFeO_{2.5}$ have been observed to be suppressed by increasing pressure up to 24 GPa (Otsuka et al., 2013). Similarly, studies of bridgmanite (H. Fei et al., 2020, 2021; Grüninger et al., 2019; Liu et al., 2017, 2019) find that although present at percent level in the uppermost lower mantle, oxygen vacancies paired with trivalent cations as $MgFeO_{2.5}$ and $MgAlO_{2.5}$ components decrease to nearly zero by ~40 GPa. Suppression of oxygen vacancies with increasing pressure may explain the slight decrease in observed concentration of Na in (Fe,Mg)O between ~30 and 50 GPa (Figure 5). However, this reaction cannot explain the substantial increase in solubility of Na in (Fe,Mg)O above 60–80 GPa.

The disproportionation of ferrous iron in Reaction 3 combines with Na_2O to produce $NaFe^{3+}O_2$. Iron disproportionation has been observed to produce Fe^{3+} in bridgmanite in the lower mantle (Frost et al., 2004; Frost &

McCammon, 2008; Swadba et al., 2023). Density functional theory computation supports substitution of $NaFeO_2$ into the oxide as an explanation for experimental observations in this work.

Paired substitution of sodium with trivalent aluminum as $NaAlO_2$ into ferropericlase has been suggested to be a dominant mechanism that can successfully model observed phase fractions and compositions in the lower mantle (Stixrude & Lithgow-Bertelloni, 2022). However, in studies by Gasparik (2000) and Brey et al. (2004), the measured amount of Na is 2–5x the amount of Al in ferropericlase, much more than can be explained by $NaAlO_2$ substitution alone. The oxide also contains iron, but the Fe^{3+} concentration was not determined by the electron microprobe analysis.

The relative stability of $NaAlO_2$ and $NaFe^{3+}O_2$ substitution in ferropericlase may differ under mantle conditions due to site occupancy of the trivalent cation and electronic spin state. Mössbauer spectroscopy indicates that some or most Fe^{3+} in periclase occupies an interstitial tetrahedral site (Hummer & Fei, 2012; Otsuka et al., 2013). In contrast, nuclear magnetic resonance shows that Al substitutes into the octahedral Mg site (McCarty & Stebbins, 2017). Both density functional theory and Mössbauer spectroscopy show that Fe^{3+} and Al occupy different sites in bridgmanite as well (Caracas, 2010; Hsu & Yu, 2012; Potapkin et al., 2013), which impacts electronic spin transitions in bridgmanite and the relative partitioning behavior of Fe^{3+} and Al between bridgmanite and ferropericlase (Badro, 2014; Lin et al., 2013). The change in the electronic structure of iron is the most significant known pressure-driven change that could be inferred to cause an increase in $NaFe^{3+}O_2$ in (Fe,Mg)O and increased sodium concentration measured at deeper mantle pressures.

Because trivalent cations exhibit a strong preference for bridgmanite (e.g., Frost & Langenhorst, 2002; Frost & McCammon, 2008; McCammon, 1997; Piet et al., 2016), the strength of this preference determines whether enough Fe^{3+} and Al can be incorporated into (Fe,Mg)O to support observed concentrations of Na and a paired substitution mechanism. In a sodium-free system, ferropericlase coexisting with aluminous bridgmanite contains only 0.1%–0.3% Al (Piet et al., 2016). The concentration of Fe^{3+} in ferropericlase measured by Piet et al. (2016) was below the detection limit of electron energy loss spectroscopy. This concentration of Fe^{3+} in ferropericlase may increase to 2%–5% for very high Fe/(Fe + Mg) compositions such as those examined in this study (Frost et al., 2001; McCammon, 1992; Nakajima et al., 2012) or with the presence of sodium as in pyrolite compositions. The presence of sodium may also affect partitioning of trivalent cations between ferropericlase and bridgmanite. Experimentalists should also consider the potential effects of reaction with the commonly used NaCl pressure-transmitting medium in design of future work.

This study can provide insights into other reactions that may apply to the crystal chemistry and thermodynamics of Na storage in Earth's lower mantle. We can rule out incorporation of chlorine in the oxide as follows: $NaCl + (Fe^{2+},Mg)O \leftrightarrow Na_x(Fe^{2+},Mg)_{1-x}O_{1-x}Cl_x$. This reaction is not consistent with experimental observations due to the absence of Cl in the oxide. However, sodium could also react with water in Earth's mantle as follows: $NaOH + (Fe,Mg)O \leftrightarrow Na_x(Fe,Mg)_{1-x}OH_x$. As ATEM also cannot provide quantitative concentrations of hydrogen in recovered samples, we have no constraints on the paired substitution of sodium and hydroxyl. Although samples used in this study were dried before loading, water absorption by the hygroscopic NaCl medium cannot be ruled out and may be a source for hydroxyl. Previous work indicates that hydroxyl solubility in ferropericlase increases with pressure and is accompanied by reduction of ferric iron to ferrous iron (Fe^{2+}) (Bolfan-Casanova et al., 2002). Further study is needed to examine the dependence of sodium and hydroxyl incorporation in the oxide on oxygen fugacity and pressure/temperature conditions due to potentially competing behaviors of iron oxidation state, oxygen vacancy concentration, and hydrogen defect concentration.

In combination, experimental and computational results are compatible with the paired substitution of sodium with Fe^{3+} in combination with other substitution mechanisms for sodium incorporation in ferropericlase. These mechanisms are depth-dependent. At shallow lower mantle pressures up to ~45–50 GPa, solubility of Na is limited to ~2–5 at% Na/(Na + Mg + Fe) and may decrease with pressure. This is consistent with the limited substitution of Na paired with trivalent cations and oxygen vacancies, the latter of which become less favorable with pressure. Our calculation results suggest that at higher pressures, the high-to-low spin transition of iron in the oxide promotes the dominance of substitution of $NaFe^{3+}O_2$ in the deeper lower mantle.

6. Implications

Throughout the lower mantle pressure range, the capacity of (Fe,Mg)O to incorporate Na exceeds the concentration of Na in average mantle. Based on the observed lower bound on solubility of sodium in (Fe,Mg)O at pressures up to ∼80 GPa, >2 at%, and a pyrolite mantle composition with ∼0.26 wt% (0.1 at%) sodium (McDonough & Sun, 1995), ferropericlase/magnesiowüstite can accommodate all of the available sodium if this phase comprises at least 5% of the lower mantle assemblage. Estimates of the composition of the average mantle agree that the phase fraction of ferropericlase exceeds this limit, although the precise amount remains a focus of ongoing study. The phase fraction of ferropericlase in the pyrolite model is estimated to be ∼16% (Dorfman, 2016). While some high-pressure elasticity measurements support the pyrolite model for the composition of the lower mantle (Criniti et al., 2021), others suggest that a better match to average seismic wave speeds is obtained for a mantle composed of ∼7%–12% ferropericlase (Mashino et al., 2020; Murakami et al., 2012). In the lowermost mantle, higher sodium solubility implies that even less ferropericlase is needed to accommodate all available sodium.

Regions of the mantle enriched in mid-ocean-ridge basalt (MORB) contain more Na than pyrolite, but also more Si. As a result MORB in the lower mantle does not contain ferropericlase, and the dominant host phase for Na is expected to be the sodium-aluminum-rich "NAL" phase or calcium-ferrite-type phase (Hirose et al., 2005; Kesson et al., 1994; Litasov & Ohtani, 2005; Ono et al., 2001; Ricolleau et al., 2010). These studies have also indicated that when ferropericlase is absent and the Na-rich calcium-ferrite-type phase is the major host for Na, bridgmanite is the next most significant Na-bearing phase containing up to ∼2 wt% Na_2O (e.g., Kesson et al., 1994). Our observations suggest that if MORB is homogenized with more mafic rock, there will be no significant Na in bridgmanite due to partitioning to the oxide. A key question to evaluating when accessory sodium-bearing phases are present and whether significant sodium is stored in ferropericlase and bridgmanite is the degree of mixing between MORB and surrounding rock and Si/Mg ratio.

Studies of the dynamics of mantle mixing have suggested that homogenized pyrolite composition may not exist in the mantle, which is proposed to be a mechanical mixture of MORB and harzburgite (Ballmer et al., 2015; Xu et al., 2008). This is supported by chemical diffusion length scales relative to mixing length scales and agreement between the physical properties of mechanical mixtures and global seismic models. However, the conditions that promote atomic mobility and equilibration, particularly the presence of melt or fluid (Hofmann & Hart, 1978), may be particularly likely to be found in hydrated subducted material and iron-rich regions at the base of the Earth's mantle. If subducted MORB or alkali-rich fluids mix and equilibrate with ultramafic surrounding mantle, there will be intermediate compositions where extra Na is present in major phases with no additional Na,Al-rich accessory phases. The equilibrium boundary between Na,Al-rich-phase-bearing MORB and other lithologies depends on the solubility of Na in major phases of pyrolite and harzburgite.

Compositions examined in this study are enriched in iron to a degree that may be found in Earth only in exceptional environments such as ultra-low velocity zones. In iron-rich chemical heterogeneities in the lowermost mantle, we would predict that high pressures and perhaps high iron content promote high solubility of sodium in magnesiowüstite. Subducted sodium-rich lithologies may react with dense iron-rich regions to produce a dynamically stable sodium reservoir in the deepest lower mantle.

7. Conclusions

ATEM analysis of iron-rich olivine compositions recovered after laser-heated diamond anvil cell experiments at conditions corresponding to the lower mantle shows that Na partitions strongly to (Fe,Mg)O relative to bridgmanite. The solubility of Na in (Fe,Mg)O is 2%–5% Na/(Na + Mg + Fe) in the shallow lower mantle and starts to increase with pressure above ∼60 GPa and reaches 6%–20% above 80 GPa. Based on our calculation results, this increase in solubility may be attributed to a high-to-low spin transition of ferric iron in the oxide: LS Fe^{3+} supports the incorporation of Na in (Fe,Mg)O as $NaFe^{3+}O_2$, while at lower pressures other substitution mechanisms such as oxygen vacancies limit the incorporation of sodium. In regions of the mantle where the Mg/Si ratio is sufficiently high for ferropericlase to be present, the sodium capacity of ferropericlase is sufficient to store all of the mantle sodium budget. Sodium enrichment in ferropericlase is expected in regions where subducted basalt or hydrous fluids carry elevated concentrations of sodium.

Conflict of Interest

The authors declare no conflicts of interest relevant to this study.

Data Availability Statement

In this work, all calculations are performed using the Quantum ESPRESSO (QE) codes, as described in Section 2 Materials and Methods. QE is an open-source package and can be downloaded for free (Giannozzi et al., 2009, 2017). Detailed information for the compilation and installation of QE can be found on the project webpage. Example input/output files of our calculations, data used to plot Figure 7, and a brief description of the data are available at Zenodo (Hsu, 2023). All composition data obtained by energy-dispersive X-ray spectroscopy and plotted in Figures 4 and 5 are available as Data Set S1.

Acknowledgments

S. M. Dorfman acknowledges the Marie Heim-Vögtlin program of the Swiss National Science Foundation for financial support through project PMPDP2_151256 and National Science Foundation EAR-1751664 and EAR-2242904. H. Hsu is supported by the National Science and Technology Council (formerly Ministry of Science and Technology) of Taiwan under Grants NSTC 112-2112-M-008-038 and 111-2112-M-008-032, and MOST 110-2112-M-008-033. H. Hsu acknowledges National Center for High-Performance Computing (NCHC) of Taiwan for computational resources. J. Badro acknowledges the financial support of the UnivEarthS Labex program at Sorbonne Paris Cité (ANR-10-LABX-0023 and ANR-11-IDEX-0005-02). GeoSoilEnviroCARS is supported by the National Science Foundation—Earth Sciences (EAR-0622171), Department of Energy—Geosciences (DE-FG02-94ER14466) and the State of Illinois.

References

Akahama, Y., & Kawamura, H. (2006). Pressure calibration of diamond anvil Raman gauge to 310 GPa. *Journal of Applied Physics*, *100*(4). https://doi.org/10.1063/1.2335683

Andrault, D., Bolfan-Casanova, N., Nigro, G. L., Bouhifd, M. A., Garbarino, G., & Mezouar, M. (2011). Solidus and liquidus profiles of chondritic mantle: Implication for melting of the Earth across its history. *Earth and Planetary Science Letters*, *304*(1–2), 251–259. https://doi.org/10.1016/j.epsl.2011.02.006

Andrault, D., Pesce, G., Bouhifd, M. A., Bolfan-Casanova, N., Hénot, J.-M., & Mezouar, M. (2014). Melting of subducted basalt at the core-mantle boundary. *Science*, *344*(6186), 892–895. https://doi.org/10.1126/science.1250466

Badro, J. (2014). Spin transitions in mantle minerals. *Annual Review of Earth and Planetary Sciences*, *42*(1), 231–248. https://doi.org/10.1146/annurev-earth-042711-105304

Ballmer, M. D., Schmerr, N. C., Nakagawa, T., & Ritsema, J. (2015). Compositional mantle layering revealed by slab stagnation at ∼1000-km depth. *Science Advances*, *1*(11), e1500815. https://doi.org/10.1126/sciadv.1500815

Birch, F. (1978). Finite strain isotherm and velocities for single-crystal and polycrystalline NaCl at high pressures and 300°K. *Journal of Geophysical Research*, *83*(B3), 1257–1268. https://doi.org/10.1029/JB083iB03p01257

Bissig, F., Khan, A., & Giardini, D. (2022). Evidence for basalt enrichment in the mantle transition zone from inversion of triplicated P- and S-waveforms. *Earth and Planetary Science Letters*, *580*, 117387. https://doi.org/10.1016/j.epsl.2022.117387

Bolfan-Casanova, N., Mackwell, S., Keppler, H., McCammon, C., & Rubie, D. C. (2002). Pressure dependence of H solubility in magnesiowüstite up to 25 GPa: Implications for the storage of water in the Earth's lower mantle. *Geophysical Research Letters*, *29*(10), 89-1–89–4. https://doi.org/10.1029/2001GL014457

Brandenburg, J. P., & van Keken, P. E. (2007). Deep storage of oceanic crust in a vigorously convecting mantle. *Journal of Geophysical Research*, *112*(B6). https://doi.org/10.1029/2006jb004813

Brey, G. P., Bulatov, V., Girnis, A., Harris, J. W., & Stachel, T. (2004). Ferropericlase—A lower mantle phase in the upper mantle. *Lithos*, *77*(1), 655–663. https://doi.org/10.1016/j.lithos.2004.03.013

Caracas, R. (2010). Spin and structural transitions in $AlFeO_3$ and $FeAlO_3$ perovskite and post-perovskite. *Physics of the Earth and Planetary Interiors*, *182*(1–2), 10–17. https://doi.org/10.1016/j.pepi.2010.06.001

Caracas, R., Hirose, K., Nomura, R., & Ballmer, M. D. (2019). Melt–crystal density crossover in a deep magma ocean. *Earth and Planetary Science Letters*, *516*, 202–211. https://doi.org/10.1016/j.epsl.2019.03.031

Chen, C., Förster, M. W., Foley, S. F., & Shcheka, S. S. (2023). Carbonate-rich crust subduction drives the deep carbon and chlorine cycles. *Nature*, *620*(7974), 576–581. https://doi.org/10.1038/s41586-023-06211-4

Christensen, U. R., & Hofmann, A. W. (1994). Segregation of subducted oceanic-crust in the convecting mantle. *Journal of Geophysical Research*, *99*(B10), 19867–19884. https://doi.org/10.1029/93jb03403

Criniti, G., Kurnosov, A., Ballaran, T. B., & Frost, D. J. (2021). Single-crystal elasticity of $MgSiO_3$ bridgmanite to mid-lower mantle pressure. *Journal of Geophysical Research: Solid Earth*, *126*(5), e2020JB020967. https://doi.org/10.1029/2020JB020967

Dorfman, S. M. (2016). Phase diagrams and thermodynamics of lower mantle materials. In H. Terasaki & R. A. Fischer (Eds.), *Deep Earth: Physics and chemistry of the lower mantle and core* (pp. 241–252). John Wiley & Sons, Inc. https://doi.org/10.1002/9781118992487.ch19/summary

Dorfman, S. M., Badro, J., Rueff, J.-P., Chow, P., Xiao, Y., & Gillet, P. (2015). Composition dependence of spin transition in $(Mg,Fe)SiO_3$ bridgmanite. *American Mineralogist*, *100*(10), 2246–2253. https://doi.org/10.2138/am-2015-5190

Dorfman, S. M., Nabiei, F., Boukaré, C.-E., Prakapenka, V. B., Cantoni, M., Badro, J., & Gillet, P. (2021). Composition and pressure effects on partitioning of ferrous iron in iron-rich lower mantle heterogeneities. *Minerals*, *11*(5), 512. https://doi.org/10.3390/min11050512

Dorfman, S. M., Prakapenka, V. B., Meng, Y., & Duffy, T. S. (2012). Intercomparison of pressure standards (Au, Pt, Mo, MgO, NaCl and Ne) to 2.5 Mbar. *Journal of Geophysical Research*, *117*(B8), B08210. https://doi.org/10.1029/2012JB009292

Dorogokupets, P. I., & Dewaele, A. (2007). Equations of state of MgO, Au, Pt, NaCl-B1, and NaCl-B2: Internally consistent high-temperature pressure scales. *High Pressure Research*, *27*(4), 431–446. https://doi.org/10.1080/08957950701659700

Fei, H., Liu, Z., Huang, R., Kamada, S., Hirao, N., Kawaguchi, S., et al. (2021). Pressure destabilizes oxygen vacancies in bridgmanite. *Journal of Geophysical Research: Solid Earth*, *126*(12), e2021JB022437. https://doi.org/10.1029/2021JB022437

Fei, H., Liu, Z., McCammon, C., & Katsura, T. (2020). Oxygen vacancy substitution linked to ferric iron in bridgmanite at 27 GPa. *Geophysical Research Letters*, *47*(6), e2019GL086296. https://doi.org/10.1029/2019GL086296

Fei, Y., Zhang, L., Corgne, A., Watson, H., Ricolleau, A., Meng, Y., & Prakapenka, V. (2007). Spin transition and equations of state of (Mg, Fe)O solid solutions. *Geophysical Research Letters*, *34*(17), L17307. https://doi.org/10.1029/2007gl030712

Feng, J., Yao, H., Wang, Y., Poli, P., & Mao, Z. (2021). Segregated oceanic crust trapped at the bottom mantle transition zone revealed from ambient noise interferometry. *Nature Communications*, *12*(1), 2531. https://doi.org/10.1038/s41467-021-22853-2

Fischer, R. A., Campbell, A. J., Shofner, G. A., Lord, O. T., Dera, P., & Prakapenka, V. B. (2011). Equation of state and phase diagram of FeO. *Earth and Planetary Science Letters*, *304*(3–4), 496–502. https://doi.org/10.1016/j.epsl.2011.02.025

Frost, D. J., & Langenhorst, F. (2002). The effect of Al_2O_3 on Fe–Mg partitioning between magnesiowüstite and magnesium silicate perovskite. *Earth and Planetary Science Letters*, *199*(1–2), 227–241. https://doi.org/10.1016/S0012-821X(02)00558-7

Frost, D. J., Langenhorst, F., & van Aken, P. A. (2001). Fe–Mg partitioning between ringwoodite and magnesiowüstite and the effect of pressure, temperature and oxygen fugacity. *Physics and Chemistry of Minerals*, *28*(7), 455–470. https://doi.org/10.1007/s002690100181

Frost, D. J., Liebske, C., Langenhorst, F., McCammon, C. A., Trønnes, R. G., & Rubie, D. C. (2004). Experimental evidence for the existence of iron-rich metal in the Earth's lower mantle. *Nature*, *428*(6981), 409–412. https://doi.org/10.1038/nature02413

Frost, D. J., & McCammon, C. A. (2008). The redox state of Earth's mantle. *Annual Review of Earth and Planetary Sciences*, *36*(1), 389–420. https://doi.org/10.1146/annurev.earth.36.031207.124322

Gale, A., Dalton, C. A., Langmuir, C. H., Su, Y., & Schilling, J.-G. (2013). The mean composition of ocean ridge basalts. *Geochemistry, Geophysics, Geosystems*, *14*(3), 489–518. https://doi.org/10.1029/2012GC004334

Garrity, K. F., Bennett, J. W., Rabe, K. M., & Vanderbilt, D. (2014). Pseudopotentials for high-throughput DFT calculations. *Computational Materials Science*, *81*, 446–452. https://doi.org/10.1016/j.commatsci.2013.08.053

Gasparik, T. (2000). Evidence for the transition zone origin of some [Mg,Fe]O inclusions in diamonds. *Earth and Planetary Science Letters*, *183*(1), 1–5. https://doi.org/10.1016/S0012-821X(00)00254-5

Giannozzi, P., Andreussi, O., Brumme, T., Bunau, O., Nardelli, M. B., Calandra, M., et al. (2017). Advanced capabilities for materials modelling with Quantum ESPRESSO. *Journal of Physics: Condensed Matter*, *29*(46), 465901. https://doi.org/10.1088/1361-648X/aa8f79

Giannozzi, P., Baroni, S., Bonini, N., Calandra, M., Car, R., Cavazzoni, C., et al. (2009). Quantum ESPRESSO: A modular and open-source software project for quantum simulations of materials. *Journal of Physics: Condensed Matter*, *21*(39), 395502. https://doi.org/10.1088/0953-8984/21/39/395502

Grüninger, H., Liu, Z., Siegel, R., Ballaran, T. B., Katsura, T., Senker, J., & Frost, D. J. (2019). Oxygen vacancy ordering in aluminous bridgmanite in the Earth's lower mantle. *Geophysical Research Letters*, *46*(15), 8731–8740. https://doi.org/10.1029/2019GL083613

Hernández, E. R., Alfè, D., & Brodholt, J. (2013). The incorporation of water into lower-mantle perovskites: A first-principles study. *Earth and Planetary Science Letters*, *364*, 37–43. https://doi.org/10.1016/j.epsl.2013.01.005

Hirose, K. (2002). Phase transitions in pyrolitic mantle around 670-km depth: Implications for upwelling of plumes from the lower mantle. *Journal of Geophysical Research*, *107*(B4). https://doi.org/10.1029/2001JB000597

Hirose, K., Takafuji, N., Sata, N., & Ohishi, Y. (2005). Phase transition and density of subducted MORB crust in the lower mantle. *Earth and Planetary Science Letters*, *237*(1–2), 239–251. https://doi.org/10.1016/j.epsl.2005.06.035

Hofmann, A. W., & Hart, S. R. (1978). An assessment of local and regional isotopic equilibrium in the mantle. *Earth and Planetary Science Letters*, *38*(1), 44–62. https://doi.org/10.1016/0012-821X(78)90125-5

Hsu, H. (2017). First-principles study of iron spin crossover in the new hexagonal aluminous phase. *Physical Review B*, *95*(2), 020406. https://doi.org/10.1103/PhysRevB.95.020406

Hsu, H. (2023). Computational data of "sodium reservoir in the deep lower mantle". [Dataset]. https://doi.org/10.5281/zenodo.10157399

Hsu, H., Blaha, P., Cococcioni, M., & Wentzcovitch, R. M. (2011). Spin-state crossover and hyperfine interactions of ferric iron in $MgSiO_3$ perovskite. *Physical Review Letters*, *106*(11), 118501. https://doi.org/10.1103/PhysRevLett.106.118501

Hsu, H., & Huang, S.-C. (2016). Spin crossover and hyperfine interactions of iron in (Mg, Fe)CO_3 ferromagnesite. *Physical Review B*, *94*(6), 060404. https://doi.org/10.1103/PhysRevB.94.060404

Hsu, H., Umemoto, K., Blaha, P., & Wentzcovitch, R. M. (2010). Spin states and hyperfine interactions of iron in (Mg,Fe)SiO_3 perovskite under pressure. *Earth and Planetary Science Letters*, *294*(1–2), 19–26. https://doi.org/10.1016/j.epsl.2010.02.031

Hsu, H., Umemoto, K., Wu, Z., & Wentzcovitch, R. M. (2010). Spin-state crossover of iron in lower-mantle minerals: Results of DFT+ U investigations. *Reviews in Mineralogy and Geochemistry*, *71*(1), 169–199. https://doi.org/10.2138/rmg.2010.71.09

Hsu, H., & Wentzcovitch, R. M. (2014). First-principles study of intermediate-spin ferrous iron in the Earth's lower mantle. *Physical Review B: Condensed Matter*, *90*(19), 195205. https://doi.org/10.1103/physrevb.90.195205

Hsu, H., Yu, Y. G., & Wentzcovitch, R. M. (2012). Spin crossover of iron in aluminous $MgSiO_3$ perovskite and post-perovskite. *Earth and Planetary Science Letters*, *359–360*(0), 34–39. https://doi.org/10.1016/j.epsl.2012.09.029

Hummer, D. R., & Fei, Y. (2012). Synthesis and crystal chemistry of Fe^{3+}-bearing (Mg,Fe^{3+})(Si,Fe^{3+})O_3 perovskite. *American Mineralogist*, *97*(11–12), 1915–1921. https://doi.org/10.2138/am.2012.4144

Irifune, T. (1994). Absence of an aluminous phase in the upper part of the Earth's lower mantle. *Nature*, *370*(6485), 131–133. https://doi.org/10.1038/370131a0

Irifune, T., Shinmei, T., McCammon, C. A., Miyajima, N., Rubie, D. C., & Frost, D. J. (2010). Iron partitioning and density changes of pyrolite in Earth's lower mantle. *Science*, *327*(5962), 193–195. https://doi.org/10.1126/science.1181443

Ishii, T., Kojitani, H., & Akaogi, M. (2019). Phase relations of harzburgite and MORB up to the uppermost lower mantle conditions: Precise comparison with pyrolite by multisample cell high-pressure experiments with implication to dynamics of subducted slabs. *Journal of Geophysical Research: Solid Earth*, *124*(4), 3491–3507. https://doi.org/10.1029/2018JB016749

Jones, T. D., Maguire, R. R., van Keken, P. E., Ritsema, J., & Koelemeijer, P. (2020). Subducted oceanic crust as the origin of seismically slow lower-mantle structures. *Progress in Earth and Planetary Science*, *7*(1), 17. https://doi.org/10.1186/s40645-020-00327-1

Kato, C., Hirose, K., Komabayashi, T., Ozawa, H., & Ohishi, Y. (2013). NAL phase in K-rich portions of the lower mantle. *Geophysical Research Letters*, *40*(19), 5085–5088. https://doi.org/10.1002/grl.50966

Kesson, S. E., Fitz Gerald, J. D., & Shelley, J. M. G. (1994). Mineral chemistry and density of subducted basaltic crust at lower-mantle pressures. *Nature*, *372*(6508), 767–769. https://doi.org/10.1038/372767a0

Kim, T., Ko, B., Greenberg, E., Prakapenka, V., Shim, S.-H., & Lee, Y. (2020). Low melting temperature of anhydrous mantle materials at the core-mantle boundary. *Geophysical Research Letters*, *47*(20), e2020GL089345. https://doi.org/10.1029/2020GL089345

Kubo, A., Ito, E., Katsura, T., Fujino, K., & Funakoshi, K. (2008). In situ X-ray diffraction of pyrolite to 40 GPa using Kawai-type apparatus with sintered diamond anvils: Possibility for the existence of iron-rich metallic particles in the lower mantle. *High Pressure Research*, *28*(3), 351–362. https://doi.org/10.1080/08957950802210486

Lin, J.-F., Speziale, S., Mao, Z., & Marquardt, H. (2013). Effects of the electronic spin transitions of iron in lower mantle minerals: Implications for deep mantle geophysics and geochemistry. *Reviews of Geophysics*, *51*(2), 244–275. https://doi.org/10.1002/rog.20010

Litasov, K. D., & Ohtani, E. (2005). Phase relations in hydrous MORB at 18–28GPa: Implications for heterogeneity of the lower mantle. *Physics of the Earth and Planetary Interiors*, *150*(4), 239–263. https://doi.org/10.1016/j.pepi.2004.10.010

Liu, Z., Akaogi, M., & Katsura, T. (2019). Increase of the oxygen vacancy component in bridgmanite with temperature. *Earth and Planetary Science Letters*, *505*, 141–151. https://doi.org/10.1016/j.epsl.2018.10.014

Liu, Z., Ishii, T., & Katsura, T. (2017). Rapid decrease of $MgAlO_{2.5}$ component in bridgmanite with pressure. *Geochemical Perspectives Letters*, *5*, 12–18. https://doi.org/10.7185/geochemlet.1739

Manning, C. E. (2004). The chemistry of subduction-zone fluids. *Earth and Planetary Science Letters*, *223*(1), 1–16. https://doi.org/10.1016/j.epsl.2004.04.030

Mao, Z., Lin, J.-F., Yang, J., Inoue, T., & Prakapenka, V. B. (2015). Effects of the Fe^{3+} spin transition on the equation of state of bridgmanite. *Geophysical Research Letters*, *42*(11), 4335–4342. https://doi.org/10.1002/2015GL064400

Mashino, I., Murakami, M., Miyajima, N., & Petitgirard, S. (2020). Experimental evidence for silica-enriched Earth's lower mantle with ferrous iron dominant bridgmanite. *Proceedings of the National Academy of Sciences*, *117*(45), 27899–27905. https://doi.org/10.1073/pnas.1917096117

Matrosova, E. A., Bobrov, A. V., Tamarova, A. P., Bindi, L., Pushcharovsky, D. Y., & Irifune, T. (2020). Sodium silicates at the boundary between the transition zone and the lower mantle: Compositional and structural patterns. *Doklady Earth Sciences*, *491*(1), 150–154. https://doi.org/10.1134/S1028334X20030113

McCammon, C. A. (1992). Magnetic properties of Fe_xO ($x > 0.95$): Variation of Néel temperature. *Journal of Magnetism and Magnetic Materials*, *104–107*, 1937–1938. https://doi.org/10.1016/0304-8853(92)91612-W

McCammon, C. A. (1997). Perovskite as a possible sink for ferric iron in the lower mantle. *Nature*, *387*(6634), 694–696. https://doi.org/10.1038/42685

McCarty, R. J., & Stebbins, J. F. (2017). Constraints on aluminum and scandium substitution mechanisms in forsterite, periclase, and larnite: High-resolution NMR. *American Mineralogist*, *102*(6), 1244–1253. https://doi.org/10.2138/am-2017-5976

McDonough, W. F., & Sun, S.-s. (1995). The composition of the Earth. *Chemical Geology*, *120*(3–4), 223–253. https://doi.org/10.1016/0009-2541(94)00140-4

Miyajima, N., Yagi, T., Hirose, K., Kondo, T., Fujino, K., & Miura, H. (2001). Potential host phase of aluminum and potassium in the Earth's lower mantle. *American Mineralogist*, *86*(5–6), 740–746. https://doi.org/10.2138/am-2001-5-614

Mulyukova, E., Steinberger, B., Dabrowski, M., & Sobolev, S. V. (2015). Survival of LLSVPs for billions of years in a vigorously convecting mantle: Replenishment and destruction of chemical anomaly. *Journal of Geophysical Research: Solid Earth*, *120*(5), 3844–3847. https://doi.org/10.1002/2014JB011688

Murakami, M., Ohishi, Y., Hirao, N., & Hirose, K. (2012). A perovskitic lower mantle inferred from high-pressure, high-temperature sound velocity data. *Nature*, *485*(7396), 90–94. https://doi.org/10.1038/nature11004

Nakagawa, T., Tackley, P. J., Deschamps, F., & Connolly, J. A. D. (2010). The influence of MORB and harzburgite composition on thermo-chemical mantle convection in a 3-D spherical shell with self-consistently calculated mineral physics. *Earth and Planetary Science Letters*, *296*(3–4), 403–412. https://doi.org/10.1016/j.epsl.2010.05.026

Nakajima, Y., Frost, D. J., & Rubie, D. C. (2012). Ferrous iron partitioning between magnesium silicate perovskite and ferropericlase and the composition of perovskite in the Earth's lower mantle. *Journal of Geophysical Research*, *117*(B8), B08201. https://doi.org/10.1029/2012JB009151

Ono, S., Ito, E., & Katsura, T. (2001). Mineralogy of subducted basaltic crust (MORB) from 25 to 37 GPa, and chemical heterogeneity of the lower mantle. *Earth and Planetary Science Letters*, *190*(1–2), 57–63. https://doi.org/10.1016/S0012-821X(01)00375-2

Otsuka, K., Longo, M., McCammon, C. A., & Karato, S. (2013). Ferric iron content of ferropericlase as a function of composition, oxygen fugacity, temperature and pressure: Implications for redox conditions during diamond formation in the lower mantle. *Earth and Planetary Science Letters*, *365*, 7–16. https://doi.org/10.1016/j.epsl.2012.11.030

Ozawa, H., Hirose, K., Tateno, S., Sata, N., & Ohishi, Y. (2010). Phase transition boundary between B1 and B8 structures of FeO up to 210 GPa. *Physics of the Earth and Planetary Interiors*, *179*(3–4), 157–163. https://doi.org/10.1016/j.pepi.2009.11.005

Piet, H., Badro, J., Nabiei, F., Dennenwaldt, T., Shim, S.-H., Cantoni, M., et al. (2016). Spin and valence dependence of iron partitioning in Earth's deep mantle. *Proceedings of the National Academy of Sciences*, *113*(40), 201605290–201611130. https://doi.org/10.1073/pnas.1605290113

Pommier, A. (2014). Interpretation of magnetotelluric results using laboratory measurements. *Surveys in Geophysics*, *35*(1), 41–84. https://doi.org/10.1007/s10712-013-9226-2

Potapkin, V., McCammon, C. A., Glazyrin, K. D., Kantor, A. P., Kupenko, I., Prescher, C., et al. (2013). Effect of iron oxidation state on the electrical conductivity of the Earth's lower mantle. *Nature Communications*, *4*(1), 1427. https://doi.org/10.1038/ncomms2436

Pradhan, G. K., Fiquet, G., Siebert, J., Auzende, A.-L., Morard, G., Antonangeli, D., & Garbarino, G. (2015). Melting of MORB at core–mantle boundary. *Earth and Planetary Science Letters*, *431*, 247–255. https://doi.org/10.1016/j.epsl.2015.09.034

Prakapenka, V. B., Kubo, A., Kuznetsov, A., Laskin, A., Shkurikhin, O., Dera, P., et al. (2008). Advanced flat top laser heating system for high pressure research at GSECARS: Application to the melting behavior of germanium. *High Pressure Research*, *28*(3), 225–235. https://doi.org/10.1080/08957950802050718

Rashchenko, S., Shatskiy, A., & Litasov, K. (2020). High-pressure Na-Ca carbonates in the deep carbon cycle. In *Carbon in Earth's interior* (pp. 127–136). American Geophysical Union (AGU). https://doi.org/10.1002/9781119508229.ch13

Ricolleau, A., Perrillat, J.-P., Fiquet, G., Daniel, I., Matas, J., Addad, A., et al. (2010). Phase relations and equation of state of a natural MORB: Implications for the density profile of subducted oceanic crust in the Earth's lower mantle. *Journal of Geophysical Research*, *115*(B8). https://doi.org/10.1029/2009JB006709

Rogmann, E.-M., Jennings, E. S., Ross, J., Miyajima, N., Walter, M. J., Kohn, S. C., & Lord, O. T. (2024). The effect of potassium on aluminous phase stability in the lower mantle. *Contributions to Mineralogy and Petrology*, *179*(5), 52. https://doi.org/10.1007/s00410-024-02129-w

Rohrbach, A., & Schmidt, M. W. (2011). Redox freezing and melting in the Earth's deep mantle resulting from carbon-iron redox coupling. *Nature*, *472*(7342), 209–212. https://doi.org/10.1038/nature09899

Sobolev, A. V., Hofmann, A. W., Kuzmin, D. V., Yaxley, G. M., Arndt, N. T., Chung, S.-L., et al. (2007). The amount of recycled crust in sources of mantle-derived melts. *Science*, *316*(5823), 412–417. https://doi.org/10.1126/science.1138113

Speziale, S., Lee, V. E., Clark, S. M., Lin, J. F., Pasternak, M. P., & Jeanloz, R. (2007). Effects of Fe spin transition on the elasticity of (Mg, Fe)O magnesiowüstites and implications for the seismological properties of the Earth's lower mantle. *Journal of Geophysical Research*, *112*(B10). https://doi.org/10.1029/2006jb004730

Stixrude, L., & Lithgow-Bertelloni, C. (2022). Thermal expansivity, heat capacity and bulk modulus of the mantle. *Geophysical Journal International*, *228*(2), 1119–1149. https://doi.org/10.1093/gji/ggab394

Sun, Y., Cococcioni, M., & Wentzcovitch, R. M. (2020). LDA+U_{sc} calculations of phase relations in FeO. *Physical Review Materials*, *4*(6), 063605. https://doi.org/10.1103/PhysRevMaterials.4.063605

Swadba, K. E., Davis, A. H., Zurkowski, C. C., Chariton, S., Prakapenka, V. B., & Campbell, A. J. (2023). Disproportionation of iron in almandine-pyrope-grossular garnet from 25 to 65 GPa. *Geochemistry, Geophysics, Geosystems*, *24*(10), e2023GC011081. https://doi.org/10.1029/2023GC011081

Tackley, P. J. (2011). Living dead slabs in 3-D: The dynamics of compositionally-stratified slabs entering a "slab graveyard" above the core-mantle boundary. *Physics of the Earth and Planetary Interiors*, *188*(3–4), 150–162. https://doi.org/10.1016/j.pepi.2011.04.013

Tateno, S., Hirose, K., & Ohishi, Y. (2014). Melting experiments on peridotite to lowermost mantle conditions. *Journal of Geophysical Research: Solid Earth*, *119*(6), 4684–4694. https://doi.org/10.1002/2013JB010616

Tauzin, B., Waszek, L., Ballmer, M. D., Afonso, J. C., & Bodin, T. (2022). Basaltic reservoirs in the Earth's mantle transition zone. *Proceedings of the National Academy of Sciences*, *119*(48), e2209399119. https://doi.org/10.1073/pnas.2209399119

Townsend, J. P., Tsuchiya, J., Bina, C. R., & Jacobsen, S. D. (2016). Water partitioning between bridgmanite and postperovskite in the lowermost mantle. *Earth and Planetary Science Letters*, *454*, 20–27. https://doi.org/10.1016/j.epsl.2016.08.009

Weiss, Y., Czas, J., & Navon, O. (2022). Fluid inclusions in fibrous diamonds. *Reviews in Mineralogy and Geochemistry*, *88*(1), 475–532. https://doi.org/10.2138/rmg.2022.88.09

Williams, Q., & Garnero, E. J. (1996). Seismic evidence for partial melt at the base of Earth's mantle. *Science*, *273*(5281), 1528–1530. https://doi.org/10.1126/science.273.5281.1528

Wood, B. J. (2000). Phase transformations and partitioning relations in peridotite under lower mantle conditions. *Earth and Planetary Science Letters*, *174*(3–4), 341–354. https://doi.org/10.1016/S0012-821X(99)00273-3

Xu, W., Lithgow-Bertelloni, C., Stixrude, L., & Ritsema, J. (2008). The effect of bulk composition and temperature on mantle seismic structure. *Earth and Planetary Science Letters*, *275*(1–2), 70–79. https://doi.org/10.1016/j.epsl.2008.08.012